Advances in Water Resources 108 (2017) 1–14

Contents lists available at ScienceDirect

Advances in Water Resources

journal homepage: www.elsevier.com/locate/advwatres

Pore-scale modeling of capillary trapping in water-wet porous media: A new cooperative pore-body filling model

L.C. Ruspini[a,*], R. Farokhpoor[a], P.E. Øren[b,c]

[a] Thermo Fisher Scientific, Norway
[b] Australian National University, Australia
[c] Petricore Norway AS, Norway

ARTICLE INFO

Article history:
Received 13 December 2016
Revised 13 June 2017
Accepted 12 July 2017
Available online 13 July 2017

Keywords:
Porous media
Two-phase flow
Capillary trapping
Residual saturation
Pore-network simulation
Cooperative pore-body filling

ABSTRACT

We present a pore-network model study of capillary trapping in water-wet porous media. The amount and distribution of trapped non-wetting phase is determined by the competition between two trapping mechanisms - snap-off and cooperative pore-body filling. We develop a new model to describe the pore-body filling mechanism in geologically realistic pore-networks. The model accounts for the geometrical characteristics of the pore, the spatial location of the connecting throats and the local fluid topology at the time of the displacement. We validate the model by comparing computed capillary trapping curves with published data for four different water-wet rocks. Computations are performed on pore-networks extracted from micro-CT images and process-based reconstructions of the actual rocks used in the experiments. Compared with commonly used stochastic models, the new model describes more accurately the experimental measurements, especially for well connected porous systems where trapping is controlled by subtleties of the pore structure. The new model successfully predicts relative permeabilities and residual saturation for Bentheimer sandstone using *in-situ* measured contact angles as input to the simulations. The simulated trapped cluster size distributions are compared with predictions from percolation theory.

1. Introduction

Multiphase flow in geological porous media is of great theoretical and practical interest in many fields of technology. Important industrial applications include geological sequestration of carbon dioxide (CO_2), remediation of non-aqueous phase liquid (NAPL) contaminants in soil and the extraction of hydrocarbons from petroleum bearing reservoirs. At the macroscopic scale, the complex physics of multiphase flow are usually described using mass balance equations for the fluids and invoking Darcy-type formulations for constitutive relationships such as relative permeability and capillary pressure (Bear, 1988; Lake, 1989). These relationships are a manifestation of the underlying pore-scale processes and depend on the micro-structure of the porous medium and the physical characteristics of the solid and the fluids that occupy the pore space (Andrew et al., 2014a; Øren and Bakke, 2003). There is therefore significant interest in pore-scale investigations aimed at computing physically-based effective properties that can be used to inform larger scale continuum models.

Capillary trapping of residual non-wetting phase (*nwp*) is of great importance to the efficiency of hydrocarbon recovery processes and is a key mechanism in long-term CO_2 geo-sequestration. In hydrocarbon recovery and in remediation processes, a minimal residual *nwp* saturation is optimal while in storage, the aim is to maximize the magnitude of trapped CO_2. Capillary trapping is also an important contributor to hysteresis in relative permeability and capillary pressure relationships (Joekar-Niasar et al., 2013; Spiteri et al., 2008). The overall amount of trapped *nwp* is governed by flowrate, wettability, pore structure and the topology of the non-wetting phase (Blunt and Scher, 1995; Herring et al., 2013; Jerauld and Salter, 1990; Øren et al., 1998).

It is generally accepted that the amount of capillary trapping for a given rock depends on the capillary number *Ca* which describes the balance between viscous and capillary forces. *Ca* has several definitions depending on the intended application (Chatzis and Morrow, 1984; Hilfer et al., 2015; Hilfer and Øren, 1996), but it has traditionally been defined in terms of a pore-scale force balance

$$Ca = \frac{v_i \mu_i}{\sigma} \quad (1)$$

* Corresponding author.
E-mail address: leonardo.c.ruspini@gmail.com (L.C. Ruspini).

http://dx.doi.org/10.1016/j.advwatres.2017.07.008
0309-1708/

where v_i is the invading phase velocity, μ_i is the invading phase viscosity and σ is the interfacial tension. For water-wet rocks, the amount of trapped *nwp* is constant at small *Ca* values, but decreases sharply if the capillary number exceeds some critical value. This is due to a transition from capillary dominated to viscous dominated flow and has been demonstrated extensively both experimentally (Armstrong et al., 2014; Chatzis and Morrow, 1984; Georgiadis et al., 2013; Khishvand et al., 2016a; Morrow et al., 1988) and numerically (Hughes and Blunt, 2000; Koroteev et al., 2013; Nguyen et al., 2006; Ramstad et al., 2014). For water-wet siliciclastic rocks such as Berea, Bentheimer and Fontainebleau the critical value has been observed to be $Ca \geq 10^{-5}$ (Khishvand et al., 2016a; Taber, 1969; Youssef et al., 2015). This value is at least one order of magnitude larger than that encountered in most reservoir scale processes such as waterflooding and in CO_2 storage situations where the natural flow of brine may only be a few meters per year (Krevor et al., 2015).

The residual *nwp* saturation depends strongly on wettability (i.e. the contact angle between the *nwp* and the solid surface). The effects of wettability on waterflood residual oil have been studied extensively in the petroleum industry. Jadhunandan and Morrow (1995) performed an extensive core-flooding study of the effects of wettability on waterflood oil recovery. They found that after injecting 20 pore volumes of brine, maximum oil recovery was achieved for weakly water-wet conditions. This has also been observed in pore-network model studies (Øren and Bakke, 2003; Valvatne and Blunt, 2004) using a pore-level scenario for wettability alteration proposed by Kovscek and Radke (1993). In the context of CO_2 sequestration, it is generally expected that the CO_2-brine-rock system will be water-wet. This is heavily supported by core-flooding experiments (Akbarabadi and Piri, 2013; 2015; Krevor et al., 2012; Niu et al., 2015; Palamara et al., 2015; Pentland et al., 2011; Suekane et al., 2008; 2009; Zuo and Benson, 2014), image-based characterization of the residual non-wetting phase and *in-situ* contact angle measurements using X-ray computed tomography (micro-CT) imaging techniques (Andrew et al., 2014a; Armstrong et al., 2012). In addition, trapped cluster sizes have been found to obey an approximate power law distribution (Andrew et al., 2014b; Favetto et al., 2010; Iglauer et al., 2011) with an exponent broadly consistent with percolation theory (Geistlinger and Mohammadian, 2015), confirming water-wet conditions.

The amount of trapping depends on the initial non-wetting phase saturation. For water-wet media, it is generally observed that the residual *nwp* saturation increases as the initial saturation increases (Land, 1968; Niu et al., 2015; Pentland et al., 2010a; Suzanne et al., 2003b). However, there is significant variation among different rocks (Al-Mansoori et al., 2010). The constitutive relation between initial and residual *nwp* saturations is commonly referred to as *IR* (initial-residual) curve. Several empirical trapping models have been developed to describe the *IR* relation. The most widely used model is that of Land (1968). It was developed to predict the *IR* characteristics of water-wet sandstones. The trapped *nwp* saturation S_{nwr} is given as

$$S_{nwr} = \frac{S_{nwi}}{1 + CS_{nwi}} \tag{2}$$

where S_{nwi} is the initial *nwp* saturation and *C* is the Land trapping coefficient. *C* is usually computed from experimental or numerical S_{nwi} and S_{nwr} values. A review of commonly used trapping models is given in Joekar-Niasar et al. (2013).

Topological and geometrical properties of the pore structure have a clear effect on the overall amount of trapping. For example, the residual gas saturation in water-wet Fontainebleau sandstone varies from $S_{gr} \simeq 0.33$ to $S_{gr} \simeq 0.9$ as porosity decreases from 0.28 to 0.05 (Bourbie and Zinzner, 1985; Suzanne et al., 2003b). Chatzis et al. (1983) investigated capillary trapping in 2D and 3D porous materials and found that the distribution and magnitude of trapped *nwp* depends strongly on the pore-throat aspect ratio. Similar findings were reported by Al-Raoush and Wilson (2005) using micro-CT imaging to analyze the distribution of residual *nwp* in a glass bead pack. The pore structure strongly affects capillary trapping because the pore-scale mechanisms underlying trapping critically depend on topological and geometrical aspects of the pore structure.

Pore-network modeling is one of the most widely used numerical tool for studying capillary dominated two-phase flow at the pore-scale (Bryant and Blunt, 1992; Fatt, 1956a; 1956b; 1956c; Øren and Bakke, 2003; Øren et al., 1998; Patzek, 2001; Ryazanov et al., 2010; Valvatne and Blunt, 2004). The predictive capabilities of network models have improved significantly with the ability to reproduce essential geometrical and topological features of the pore space using networks extracted from micro-CT images (Dong and Blunt, 2009; Lindquist and Venkatarangan, 1999; Lindquist et al., 2000; Silin and Patzek, 2006) or process-based reconstructions (Bakke and Øren, 1997; Øren and Bakke, 2002; 2003). Pentland et al. (2010b) successfully computed capillary trapping for an n-decane/brine system in water-wet Berea and Clashach sandstones using pore-networks extracted from micro-CT images. In order to match residual saturations, the advancing contact angle θ_a had to be tuned and was randomly distributed in the range 27°–87°. This is high for a strongly water-wet system. Raeini et al. (2015) found that pore-network simulations with $\theta_a = 47°$ significantly over-estimated trapping in water-wet sandpacks while direct finite volume simulations better matched the experimental data. Bondino et al. (2013) reported that contact angles had to be adjusted to unrealistically high values in order to match experimentally measured residual saturations in water-wet systems. Similar findings were reported by Valvatne and Blunt (2004).

The failure of pore-network models to predict residual saturations for water-wet systems is typically attributed to the simplified geometry, the presence of viscous forces, or to overestimation of snap-off events (Valvatne and Blunt, 2004). However, predictive capabilities of pore-network models do not only depend on the ability to reproduce wettability effects and to capture essential geometrical and topological features of the pore space. They also depend on a precise characterization of the pore-scale displacement and trapping mechanisms. Pore-scale mechanisms for imbibition were first observed in two-dimensional micro-model experiments and described in the pioneering works of Lenormand et al. (1983) and Lenormand and Zarcone (1984). There are three basic types of displacements: piston-like, snap-off and cooperative pore-body filling. Recently, these mechanisms have been observed in rocks using high speed synchrotron-based micro-CT (Andrew et al., 2015; Armstong and Berg, 2013; Berg et al., 2013).

Piston-like (PL) advance refers to the displacement of non-wetting phase from a throat by an invading interface initially located in an adjoining wetting phase filled pore-body. The invading wetting phase preferentially fills the narrowest regions of the pore space. Piston-like displacement in throats is favored while wetting phase advance is impeded by the larger pore-bodies. Piston-like advance is not a bond-breaking mechanism (i.e. local *nwp* disconnection) and it does not result in trapping of the non-wetting phase.

Snap-off (SO) refers to the invasion of a non-wetting phase filled throat by arc menisci (AM) or wetting layers initially present in corners, crevices and rough surfaces of the pore space. For small injection velocities, wetting layers will swell and thicken ahead of the bulk wetting phase invasion in pores and throats. At a critical capillary pressure, the AMs fuse and the center of the throat spontaneously fills with wetting phase (Roof, 1970). Snap-off is a bond-breaking mechanism that can lead to *nwp* trapping.

Cooperative pore-body filling (PBF) refers to cases where wetting phase displaces non-wetting phase from a pore-body when one or more of the connecting throats are filled with non-wetting phase. Using the terminology of Lenormand et al. (1983), the displacement events are labeled I_n where n is the number of connecting throats filled with non-wetting phase. The I_1 is not a bond-breaking mechanism. In contrast, for $n > 1$, the I_n displacements are bond-breaking mechanisms that can lead to *nwp* trapping.

At the pore-scale, the amount and distribution of trapped *nwp* are determined by the competition between the two bond-breaking mechanisms, SO and PBF. The mechanism that actually dominates depends on pore-structure, contact angle and the topology of the non-wetting phase (Herring et al., 2013; Øren et al., 1998; Valvatne and Blunt, 2004). Snap-off can lead to significant trapping while PBF encourages a flat, frontal advance of the wetting phase with little trapping, at least for uniform porous media such as the micro-model experiments described by Lenormand et al. (1983).

Fluid topology, phase connectivity and capillary entry pressures govern the order in which the wetting phase invades pores and throats (Øren et al., 1998). The PL and SO mechanisms are well characterized and capillary entry pressures can be calculated from local geometrical and wetting characteristics (Blunt and Scher, 1995; Øren et al., 1998). In contrast, PBF depends on fluid topology and there is no exact expression for the capillary entry pressure for different I_n configurations. Typically, stochastic expressions are used to compute these entry pressures (Blunt, 1997; Øren et al., 1998). Clearly, this is a simplification that can limit the predictive capabilities of pore-network models, especially for rocks where PBF is an important trapping mechanism.

This paper presents a new model for the calculation of capillary entry pressures for cooperative pore-body filling. The model accounts for wetting properties, geometrical characteristics of the pore-body and the spatial locations of the connecting *nwp* filled throats. The new PBF model is implemented in a pore-network simulator described earlier (Øren et al., 1998). We compute capillary trapping curves for different water-wet rocks and compare the results with experimental data. The simulated trapped cluster size distributions are compared with predictions from percolation theory.

2. Previous PBF models

Capillary entry pressure for pore-body filling is limited by the largest radius of curvature required to invade a pore-body. For a pore-body with coordination number z, there are $z-1$ possible displacements, referred to as I_1 to I_{z-1}. If only one of the connecting throats is filled with non-wetting phase, the I_1 displacement is similar to a piston-like displacement and the capillary entry pressure can be calculated from an energy balance using the Mayer, Stowe and Princen (MSP) theory (Mayer and Stowe, 1965; Princen, 1969). However, when two or more of the adjacent throats are occupied by the non-wetting phase, the radius of curvature depends on the spatial locations of the *nwp* filled throats (Lenormand et al., 1983). Blunt (1997) presented a stochastic model for the radius of curvature based on the number n of adjacent *nwp* filled throats, represented as

$$R_n = \frac{1}{\cos\theta_a}\left(r_p + \sum_{i=1}^{n} A_i x_i\right) \tag{3}$$

where x_i are random numbers between 0 and 1, A_i are empirical parameters ({0, 2.5, 5, 20, 100} μm), θ_a is the advancing contact angle and r_p is the pore-body radius. This model is referred to as Blunt_1 in the following.

Øren et al. (1998) presented a variation of Eq. (3) by modifying the A_i parameters to also depend on the radii of the *nwp* filled throats

$$R_n = \frac{1}{\cos\theta_a}\left(r_p + \sum_{i=1}^{n} a_i r_i x_i\right) \tag{4}$$

where the values of a_i are given by {0.0, 0.5, 1, 2, 5, 10} and r_i are the radii of the *nwp* filled throats. We refer to this model as Oren_1. The entry capillary pressure is given by $Pc_n = 2\sigma/R_n$. Additional variations on the initial stochastic model can be found in the literature (Patzek, 2001).

To account for the possibility of negative capillary entry pressures for $\theta_a < 90°$, Blunt (1998) proposed to define the entry capillary pressure as

$$Pc_n = \frac{2\sigma\cos(\theta)}{r_p} - \sigma\sum_{i=1}^{n} A_i x_i \tag{5}$$

where the coefficient $A_i = 1500\ \frac{1}{m}$. This model is referred to as Blunt_2. Valvatne (2004) presented a variation of the Blunt_2 model by relating the parameter A_i to the permeability k of the pore-network

$$Pc_n = \frac{2\sigma\cos(\theta)}{r_p} - \sigma\frac{0.03}{\sqrt{k}} \tag{6}$$

This last model is referred to as Valvatne_1. No analysis of the differences between these models has been presented in the literature. As part of this work, we present a systematic comparison of the effects that the different stochastic models have on capillary trapping in water-wet rocks.

3. New PBF model

In this section we derive a new model for calculating capillary entry pressures for cooperative pore-body filling. In contrast to the stochastic PBF models described earlier, the new model accounts for the local fluid topology and the geometrical characteristics of the throats actually involved in the displacement. The model is based on the following geometrical assumptions: (i) the center-line of the throats connected to a pore-body meet in the center of the pore-body, (ii) the limiting radius of curvature is governed by the pair of *nwp* filled throats with the largest angular spacing, and (iii) the radius of curvature is calculated in the plane defined by the center-line of the two throats and the pore-body center. In the next section, we demonstrate the key steps involved in the calculations of PBF entry pressures assuming a symmetric pore-throat system, i.e. constant throat size and constant contact angle. The analysis is then extended to the general case, i.e. different throat sizes and different contact angles.

3.1. Symmetric pore-throat system

Fig. 1 shows a schematic of a symmetric pore-throat system. The radius of curvature can be expressed as

$$R_n = f(\alpha, \theta, r_t, r_p) \tag{7}$$

where α is the angle between the throats, θ is the contact angle, r_t is the throat radius (equal for both) and r_p is the pore radius. α is calculated from the position of the pore and throat centers using the cosine rule

$$\cos(\alpha) = \frac{\overrightarrow{C_pC_i}\cdot\overrightarrow{C_pC_j}}{\left|\left|\overrightarrow{C_pC_i}\right|\right|\left|\left|\overrightarrow{C_pC_j}\right|\right|} \tag{8}$$

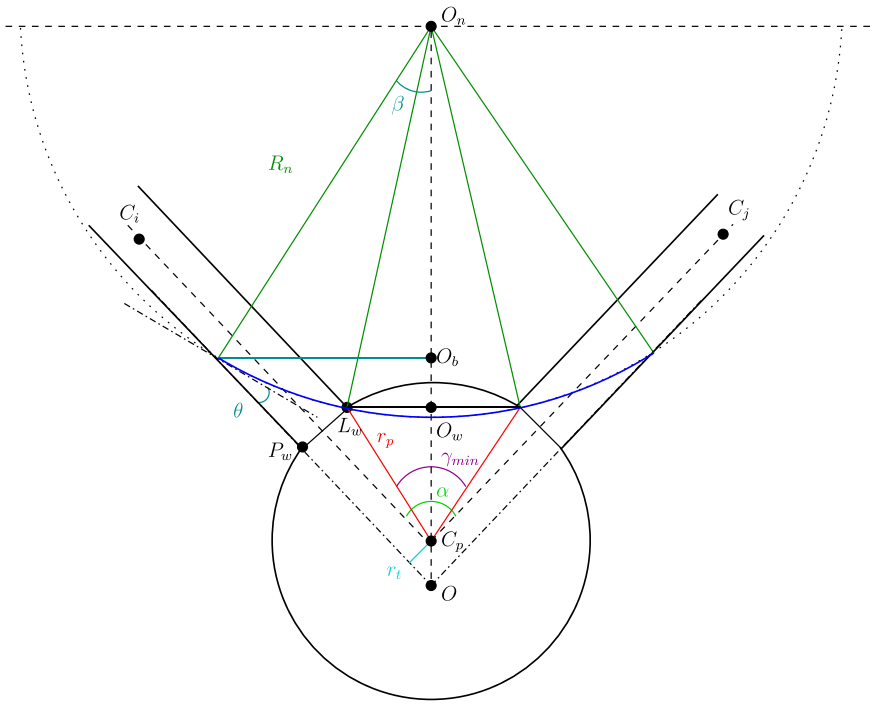

Fig. 1. Geometrical description of a symmetric pore-throat system.

where C_p, C_i, C_j are the center points of the pore and the two throats, respectively. In addition, the angles γ_{min}, γ_{max} and β are defined as

$$\gamma_{min} = \alpha - 2\arcsin\left(\frac{r_t}{r_p}\right) \tag{9}$$

$$\gamma_{max} = \alpha + 2\arcsin\left(\frac{r_t}{r_p}\right) \tag{10}$$

$$\beta = \frac{\pi}{2} - \theta - \frac{\alpha}{2} \tag{11}$$

An important assumption of the model is the position where the interface becomes unstable. The two limiting cases are: the *non-invasive* limit in which the interface becomes unstable once it enters into the throat region (point P_w in Fig. 1); and the completely *invasive* limit in which the interface becomes unstable when it touches the upper limit of the throat wall (point L_w in Fig. 1). The angle γ defines the position where the interface becomes unstable and is given by

$$\gamma = \epsilon\ \gamma_{min} + (1-\epsilon)\ \gamma_{max} \tag{12}$$

where ϵ is a model parameter ranging from 0.0 to 1.0.

As shown in Fig. 1, there are two points where the meniscus intersects the pore-throat border. It is readily shown that

$$OO_n = OO_b + O_bO_n = OC_p + C_pO_w + O_wO_n \tag{13}$$

$$OO_b = \frac{R_n\sin(\beta)}{\tan\left(\frac{\alpha}{2}\right)};\quad O_bO_n = R_n\cos(\beta);$$
$$OC_p = \frac{r_t}{\sin\left(\frac{\alpha}{2}\right)};\quad C_pO_w = r_p\cos\left(\frac{\gamma}{2}\right) \tag{14}$$

$$O_wO_n^2 = R_n^2 - \left(r_p\sin\left(\frac{\gamma}{2}\right)\right)^2 \tag{15}$$

and the radius of curvature R_n can be calculated by solving the following quadratic equation

$$\mathrm{a}\,\mathrm{R_n^2} + \mathrm{b}\,\mathrm{R_n} + \mathrm{c} = 0 \tag{16}$$

$$\mathrm{a} = \left(\cos(\beta) + \frac{\sin(\beta)}{\tan\left(\frac{\alpha}{2}\right)}\right)^2 - 1$$
$$\mathrm{b} = -2\left(\cos(\beta) + \frac{\sin(\beta)}{\tan\left(\frac{\alpha}{2}\right)}\right)\left(\frac{\mathrm{r_t}}{\sin\left(\frac{\alpha}{2}\right)} + \mathrm{r_p}\cos\left(\frac{\gamma}{2}\right)\right)$$
$$\mathrm{c} = \left(\frac{\mathrm{r_t}}{\sin\left(\frac{\alpha}{2}\right)} + \mathrm{r_p}\cos\left(\frac{\gamma}{2}\right)\right)^2 + \left(\mathrm{r_p}\sin\left(\frac{\gamma}{2}\right)\right)^2$$

From Eq. (16) it is possible to calculate the limiting radius of curvature and then obtain the entry capillary pressure by using

$$\mathrm{Pc_n} = 2\frac{\sigma}{\mathrm{R_n}} \tag{17}$$

3.2. Non-symmetric system: different throat sizes

If the throats have different radii, it is always possible to map the system onto an equivalent symmetric system. Fig. 2 shows the geometrical relations between a non-symmetric throat system and its equivalent symmetric system. The radius of curvature is the same in both systems. The smallest throat determines the interface position in the non-symmetric system and it is used as the throat radius in the equivalent symmetric system. The angle between the two throats α and the contact angle θ are the same in both systems. For the non-symmetric system shown in Fig. 2, we have

$$\alpha_1 + \alpha_2 = \alpha \tag{18}$$

$$\frac{\sin(\alpha_1)}{\sin(\alpha_2)} = \frac{r_1}{r_2} \tag{19}$$

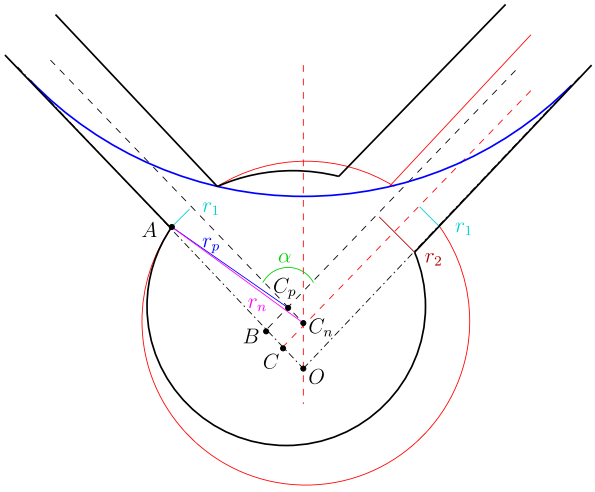

Fig. 2. Geometrical description of a non-symmetric two throats system and its associated symmetric system. The blue line represents the interface position for the new PBF model.

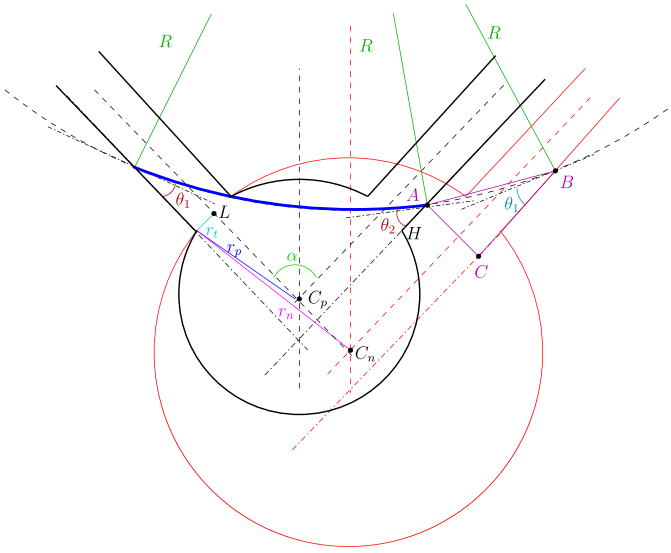

Fig. 3. Geometrical description of a non-symmetric two throats system with different contact angles and its equivalent symmetric system.

$$\tan(\alpha_1) = \frac{\sin(\alpha)}{\left(\frac{r_2}{r_1} + \cos(\alpha)\right)} \tag{20}$$

where α_1 and α_2 are the angles defined by the throats axes and the segment OC_p. For both systems the distance AO is the same and

$$AB^2 = r_p^2 - r_1^2 \tag{21}$$

$$AC = AB + \frac{r_1}{\tan(\alpha_1)} - \frac{r_1}{\tan(\alpha/2)} \tag{22}$$

Finally, the pore radius of the equivalent symmetric system is given by

$$r_p^* = \sqrt{AC^2 + r_1^2} \tag{23}$$

In summary, for a non-symmetric throat system it is always possible to derive an equivalent symmetric system having the same radius of curvature. The equivalent throat radius is given by the minimum of the two throat radii, the angle between the throats is the same and the equivalent pore size is given by Eq. (23). Once these new parameters are calculated, the radius of curvature can be determined from Eq. (16).

3.3. Non-symmetric system: different contact angles

An equivalent symmetric system can also be obtained for cases where the contact angles are different in the two throats. A geometrical representation of this case and its equivalent symmetric system is shown in Fig. 3. Similarly to the analysis presented above, the throat that defines the position of the interface is the one with the smallest contact angle. This is the contact angle used in the equivalent symmetric system. From Fig. 3, we have

$$AB = 2R\ \cos\left(\frac{\theta_{max} - \theta_{min}}{2}\right) \tag{24}$$

$$AC = AB\ \cos\left(\frac{\theta_{max} + \theta_{min}}{2}\right) \tag{25}$$

where the distance AC is the difference between the pore center in both systems. The equivalent pore radius is given by

$$LC_p = \sqrt{r_p^2 - r_t^2} \tag{26}$$

$$r_p^* = \sqrt{(LC_p + AC)^2 + r_t^2} \tag{27}$$

It is important to note that the new equivalent pore size r_p^* depends on the interface radius R_n and cannot be determined analytically. It must be computed iteratively by solving Eqs. (27) and (16). During this iterative process, it is necessary to check that the interface is still located inside the throats because for some numerical conditions it can be located at the throat/pore border.

The key difference between the new pore-body filling model described in this section and the stochastic models discussed above, is that the new model accounts for the spatial locations of the *nwp* filled throats actually involved in the displacement. This means that the radius of curvature depends on the local fluid topology which changes during the simulation. Entry pressures for PBF can therefore not be calculated prior to the simulations.

4. Materials and methods

We compare simulated capillary trapping curves with experimental data for four different water-wet rocks. Table 1 lists the fluids and rock properties of the experimental data sets. Pore space representations of the rocks are obtained from micro-CT imaging (sandpack and Bentheimer) and process-based reconstructions (Fontainebleau and Berea). A total of 12 pore space images are analyzed. Table 2 summarizes the properties of the images. Absolute permeabilities (LB k) are calculated using a D3Q19 lattice Boltzmann solver (Øren et al., 2007) with multiple relaxation times. Formation factors (FD FRF) are computed by solving a Finite Difference discretization of the Laplace equation assuming insulating pore walls Øren and Bakke (2002).

We generated pore-network representations of the pore space images using e-Core.[1] Details about the algorithms used to extract topological and geometrical characteristics of the networks are given elsewhere (Bakke and Øren, 1997; Øren and Bakke, 2003; Øren et al., 1998). Table 3 lists important geometrical and topological properties of the networks. The average aspect ratio $\overline{AR}$ is de-

[1] Digital Rock Laboratory by Thermo Fisher Scientific (formerly FEI).

Table 1
Properties of samples and fluids used in experimental imbibition studies.

Reference	Samples	ϕ [%]	k [mD]	*nwp*/*wp*	ρ_{wp}[a]	ρ_{nwp}[a]	σ[b]
Pentland et al. (2010a)	Sandpack	37	32,000	octane/brine	1042	709	50.81
Suzanne et al. (2003b)	Fontainebleau	3–28	0.1–3000	air/water	770	2	24
Kumar et al. (2009)	Fontainebleau	13.5	1,800	butane/brine	–	–	40
Pentland et al. (2011)	Berea	22	466	nDecane/brine	1,025	700	–
Niu et al. (2015)	Berea	21	212	CO2/brine	1,023	386	36–44
Akbarabadi and Piri (2013)	Berea	20	50	CO2/brine	1,123	393	38.15
Oak (1990)	Berea	–	1,000	dodecane/brine	1,001	802	53
Alizadeh and Piri (2014)	Bentheimer	21.7	2,660	soltrol/brine	1,138	802	40.7
Raeesi et al. (2013)	Bentheimer	23	1,980	decane/brine	1,000	691	58

[a] Density [kg/m^3]
[b] Interfacial Tension [mN/m]

Table 2
Pore space images and digital properties of rock samples used in the pore-scale simulations. Δ is the voxel length, Size is the dimensions of the image (voxels), LB k is the grid based Lattice Boltzmann permeability, FD FRF is the grid based Finite Difference formation factor, PNM k is the pore-network permeability and PNM FRF is the pore-network formation factor.

Sample	Δ[μm]	Size	Porosity [%]	LB k [mD]	FD FRF	PNM k [mD]	PNM FRF
Sandpack	10	450^3	36.3	39,055	5.05	37,560	4.25
Bentheimer	2.03	800^3	21.4	3,260	12.86	3,116	12.7
Berea	1.5	$1{,}200^3$	21.7	543.9	14.37	551.5	10.6
Fontainebleau_1	2.76	$1{,}000^3$	24.9	5,786	9.02	5,545	7.25
Fontainebleau_2	2.76	$1{,}000^3$	21.9	3,837	11.69	3,556	9.48
Fontainebleau_3	2.76	$1{,}000^3$	19.9	2,696	14.65	2,465	11.7
Fontainebleau_4	2.76	$1{,}000^3$	17.9	1954	18.63	1,846	14.5
Fontainebleau_5	2.76	$1{,}000^3$	14.9	1,073	27.79	940.6	22.2
Fontainebleau_6	2.76	$1{,}000^3$	12.9	632.4	40.48	557.6	31.7
Fontainebleau_7	2.76	$1{,}000^3$	9.8	228.8	82.36	206.6	64.5
Fontainebleau_8	2.76	$1{,}000^3$	7.8	88.91	175.7	69.6	139
Fontainebleau_9	2.76	$1{,}000^3$	4.3	8.78	1105.4	1.38	1,340

Table 3
Geometrical and topological properties of the pore-networks. $\bar{r}_p$ is the average pore size, $\bar{r}_t$ is the average throat size, $\overline{AR}$ is the average aspect ratio and $\bar{z}$ is the average coordination number.

Sample	Porosity [%]	Pores	Throats	$\bar{r}_p$ [μm]	$\bar{r}_t$ [μm]	$\overline{AR}$	$\bar{z}$
Sandpack	36.3	18,824	52,867	39.1	24.0	2.00	5.55
Bentheimer	21.4	5,052	9,380	14.4	9.66	2.12	3.80
Berea	21.7	86,155	219,923	7.35	3.98	2.71	5.06
Fontainebleau_1	24.9	23,719	61,108	22.6	13.0	2.44	5.14
Fontainebleau_2	21.9	25,979	63,155	21.1	12.1	2.52	4.84
Fontainebleau_3	19.9	27,125	63,649	20.0	11.5	2.54	4.61
Fontainebleau_4	17.9	27,373	61,945	19.0	11.0	2.58	4.46
Fontainebleau_5	14.9	27,502	58,581	17.8	10.3	2.58	4.16
Fontainebleau_6	12.9	26,112	53,389	17.2	9.91	2.61	3.99
Fontainebleau_7	9.9	23,701	44,734	16.0	9.26	2.58	3.66
Fontainebleau_8	7.8	20,838	37,025	15.4	8.79	2.61	3.41
Fontainebleau_9	4.3	15,335	24,096	11.6	7.09	2.73	3.02

Table 4
In-situ contact angle measurements for binary-equilibrated two-phase experiments in Berea and Bentheimer sandstone.

Reference	Sample	*nwp*/*wp*	θ_r [°]	θ_a [°]
Aghaei and Piri (2015)	Bentheimer	nDecane/brine	10–30	20–42
Aghaei and Piri (2015)	Berea	soltrol/brine	6–26	7–55
Khishvand et al. (2016a)	Bentheimer	nDecane/brine	17–32	20–50
Khishvand et al. (2016b)	Berea	decalin/brine	37–56	44–71
Khishvand et al. (2016b)	Berea	N_2/brine	28–44	35–58
Khishvand et al. (2016b)	Berea	N_2/decalin	28–48	37–56

fined as

$$\overline{AR} = \frac{1}{N}\sum_{i=1}^{N}\frac{r_{p,i}}{\bar{r}_{t,i}} \tag{28}$$

where N is the total number of pores, $r_{p,i}$ is the size of the pore i and $\bar{r}_{t,i}$ is the average size of the throats connected to pore i. Computed permeabilities and formation factors of the pore-networks are compared with the image-based results in Table 2. The properties are in good agreement with both the grid calculations performed directly on the pore space images and the corresponding experimental results.

Pore-network models require contact angles as input to the simulations. Measurements of *in-situ* contact angles using micro-CT imaging techniques is a unique and promising method for measuring effective contact angles. The application of this method to a wide variety of rocks is of course limited by the ratio of the pore to voxel size. Unless this ratio is large, voxelation errors can lead to significant measurement uncertainties. *In-situ* contact angle mea-

surements have recently been reported for Bentheimer and Berea sandstones (Aghaei and Piri, 2015; Khishvand et al., 2016a; 2016b). The results of these measurements are summarized in Table 4.

The contact angle distributions for the two measurement series in Bentheimer sandstone are similar with a mean advancing contact angle $\theta_a \simeq 33^\circ$. For Berea sandstone, the mean value for the two oil-water systems is $\theta_a \simeq 31^\circ$ (soltrol-brine) and $\theta_a \simeq 57^\circ$ (decalin-brine). The contact angle distribution for the gas-oil and gas-water systems are similar with a mean $\theta_a \simeq 46^\circ$.

5. Results and discussion

A pore-network simulator was developed following the model described in Øren et al. (1998). All the stochastic PBF models as well as the new model were included in the pore-network simulator. A detailed description of the simulator and the calculations of relative permeability and capillary pressure are given elsewhere (Øren et al., 1998). We use $\epsilon = 0.5$ see Eq. (12), for all the simulations presented in this work. Appendix A shows that the exact value of ϵ has little effect on the amount of trapping.

We computed capillary trapping curves using both the new PBF model and the four stochastic models presented in Section 2. The observed differences between the models are analyzed. We compare the simulated results with the corresponding experimental data sets listed in Table 1. The input fluid properties are the same as those reported in the experiments. We assume strongly water-wet conditions for all primary drainage simulations, randomly assigning a receding contact angle θ_r in the range 0°–10°. Based on the measurements listed in Table 4, we use a random uniform distribution for θ_a between 30° and 35° as the base case input when simulating imbibition. We perform a sensitivity analysis of the impact of the advancing contact angle on capillary trapping using contact angles in the range 15°–20° and 45°–50°.

5.1. Capillary trapping in sandpack LV60A

Pentland et al. (2010a) measured residual oil saturation S_{or} as a function of initial oil saturation S_{oi} in a sandpack at ambient conditions. The sandpack was initially fully saturated with brine and then different volumes of oil (octane) were injected. Equilibrium initial conditions were established by letting the oil rise under buoyancy forces. The sandpack was then flooded with brine at low Ca to establish S_{or}. The sample was sliced into 10 sections and trapped saturations were measured using gas chromatography.

We extracted a pore-network from micro-CT images of the actual sandpack used in the experiments (LV60A). Properties of the images and the pore-network are given in Table 2. We established S_{oi} by simulating a primary drainage process. Oil is injected at the inlet face of the network and water escapes through the outlet on the opposite side. The simulation stops when the oil saturation reaches the target value, S_{oi}. Next, we simulate an imbibition process by injecting water. To mimic the experimental boundary conditions, oil is allowed to leave the network through both the inlet and outlet faces. The simulation stops when oil is no longer connected to the outlet faces.

Fig. 4 compares simulated trapping curves with the experimental measurements. Each data point of this IR curve corresponds to one simulation sequence. The stochastic models clearly overestimate the amount of trapping (by more than 100% in several cases). This is similar to the results reported by Raeini et al. (2015). In contrast, the results for the new PBF model match the experimental data with less than 10% deviation across the entire saturation range. The simulated trapping curve increases almost linearly with initial saturation until a maximum $S_{or} \simeq 0.14$ is reached at $S_{oi} \simeq 0.55$. The trapped saturation remains constant as S_{oi} increases further. As observed in Fig. 4, the best-fit to Land's trapping model

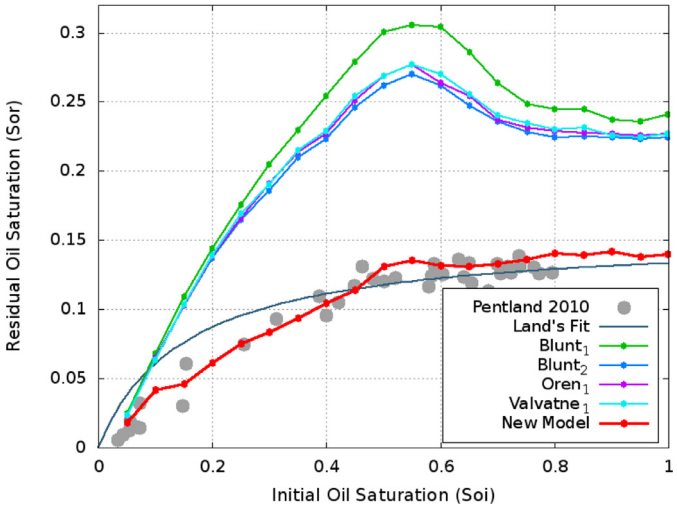

Fig. 4. Capillary trapping in sandpack LV60. Comparison between experimental (Pentland et al., 2010a), stochastic models ($Blunt_1$, $Blunt_2$, $Oren_1$ and $Valvatne_1$) and the new cooperative pore-body filling model results. The best fit for Land's trapping model is plotted with a dark blue line.

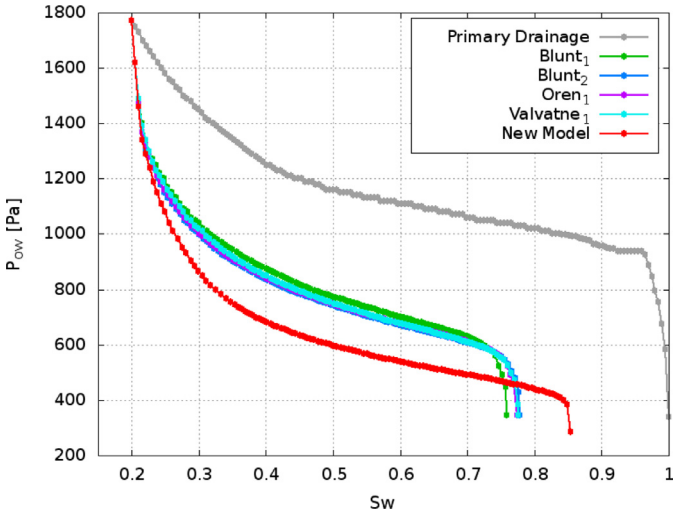

Fig. 5. Capillary pressure curves in a sandpack sample for the different pore-body filling models when $S_{oi} = 0.8$.

does not predict this behavior (Pentland et al., 2010a). The simulated results display percolation threshold effects at small initial saturations ($S_{oi} < 0.2$) as the distribution of S_{oi} is not uniform.

Generally, the new PBF model predicts lower capillary entry pressures than the stochastic models. This is supported by Fig. 5 which shows imbibition capillary pressure curves for $S_{oi} \simeq 0.8$. The capillary pressure curve for the new PBF model is lower than those for the stochastic models, suggesting that the dominant pore-scale displacement mechanism is different. This is confirmed by analyzing the displacement statistics. At $S_{oi} \simeq 0.8$, the ratio of snap-off to PBF events is 9.4 for the new model. For the stochastic models this value is around 0.4. Snap-off is the dominant bond-breaking mechanism for the new model, while PBF dominates for the stochastic models. However, the residual saturation is considerably smaller for the new model. This is not in agreement with the commonly held view that snap-off leads to significant trapping while cooperative pore-body filling leads to very little trapping.

The key to understand these seemingly counter-intuitive results lies in how subtleties of the pore structure control the competition between snap-off and piston-like advance. The sandpack is

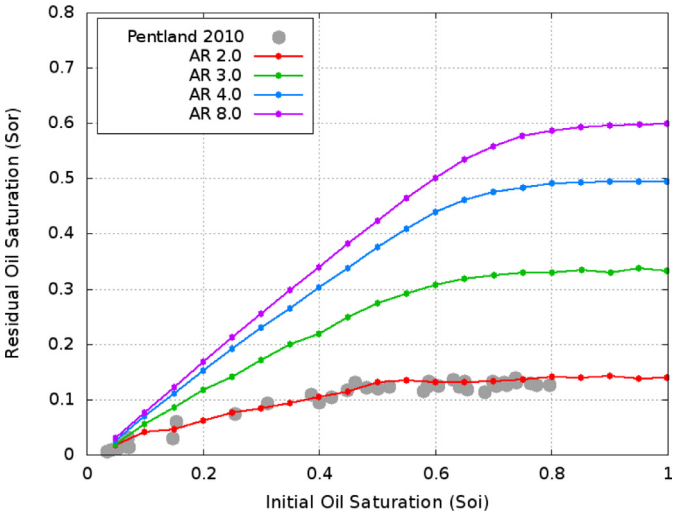

Fig. 6. Sensitivity analysis of pore-throat aspect ratio on capillary trapping for a sandpack sample using the new PBF model.

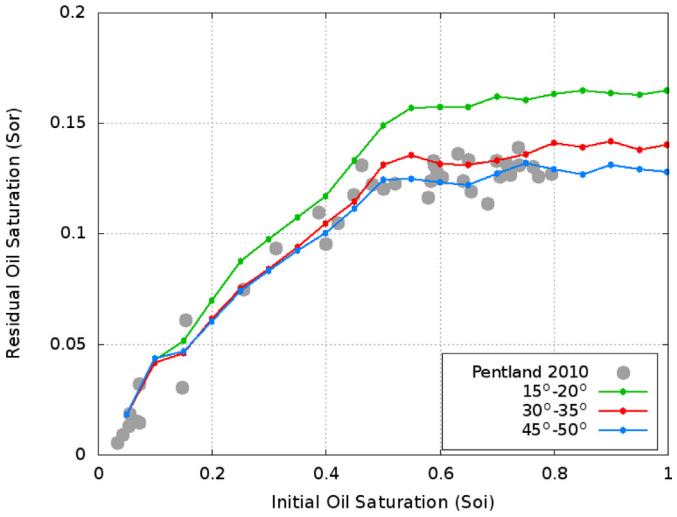

Fig. 7. Sensitivity analysis of advancing contact angles on capillary trapping for the sandpack sample, compared with experimental data from Pentland et al. (2010a).

well connected ($\tilde{z} = 5.6$) and has a low aspect ratio ($\overline{AR} \simeq 2.0$). For most of the I_n configurations established, the maximum angle α between *nwp* filled throats is large and the PBF entry pressure is small. The wetting phase advance is arrested at pore bodies. It proceeds by snap-off in the smallest connecting throats until an I_1 configuration (PBF with only one *nwp* filled throat) is established. The remaining *nwp* filled throat is the largest of the connecting throats. It is this pore-throat aspect ratio that determines if trapping in the pore body will occur. For rocks with low aspect ratios, there is a subtle balance between I_1 invasion and snap-off in the connecting throats (Øren et al., 1998; Valvatne and Blunt, 2004). If the aspect ratio is small, the I_1 entry pressure is greater than for snap-off. In this case, the wetting phase invades the pore and adjoining throat by piston-like displacements and there is no trapping. If the aspect ratio is large, snap-off is the preferred displacement, resulting in trapping of the *nwp* in the pore-body.

This is confirmed in Fig. 6 which illustrates the effects of the average aspect ratio on the sandpack trapping curve. We changed the aspect ratio by uniformly reducing the throats sizes while keeping the pore sizes and the network topology unchanged. The maximum trapped saturation (at $S_{oi} \simeq 1$), increases from $S_{or} \simeq 0.14$ to $S_{or} \simeq 0.34$ as the $\overline{AR}$ increases from 2.0 to 3.0. For $\overline{AR} = 4.0$, the maximum trapped saturation increases to 0.5, clearly demonstrating that the competition between snap-off and piston-like I_1 advance strongly depends on the pore-throat aspect ratio.

Fig. 7 shows computed trapping curves for three sets of advancing contact angles: 15°–20° 30°–35° and 45°–50°. The maximum trapped saturation depends on the contact angle and increases from $S_{or} \simeq 0.12$ to $S_{or} \simeq 0.17$ as the contact angle decreases from 45°–50° to 15°–20°. This is due to changes in the competition between snap-off and PBF displacements. Capillary entry pressures for snap-off decrease faster with increasing contact angles than the PBF entry pressures. Snap-off is impeded and I_1 and cooperative pore-body filling displacements (frontal advance) increase, reducing trapping.

5.2. Capillary trapping in Fontainebleau sandstone

Bourbie and Zinzner (1985) measured trapped gas saturation S_{gr} as a function of porosity in Fontainebleau sandstone samples. In the experiments, clean dried samples were placed on a bed of glass beads filled with toluene. Toluene spontaneously imbibed in the core plug until it reached an equilibrium state. Toluene saturation was inferred from weight measurements before and after imbibition. The same technique was employed by Suzanne et al. (2003b) but the experimental set-up was placed in a closed system filled with liquid vapor saturated air.

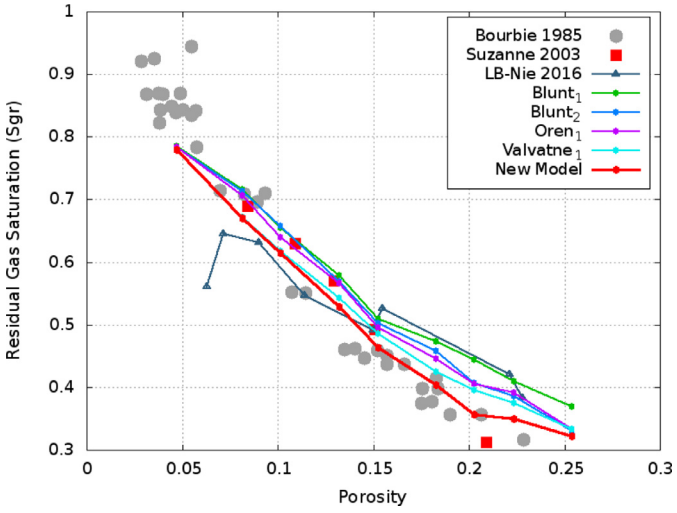

Fig. 8. Capillary trapping as a function of porosity for Fontainebleau sandstone samples. Comparison between experimental results (Bourbie and Zinzner, 1985; Suzanne et al. 2003b), pore-network simulations (stochastic models and the new cooperative pore-body filling mechanism) and lattice-Boltzmann simulations (Nie et al., 2016).

We reconstructed nine process-based models of Fontainebleau sandstone. The porosity of the models ranged from 0.043 to 0.249. Details about the reconstruction algorithm are given elsewhere (Bakke and Øren, 1997; Øren and Bakke, 2002). Input grain sizes were measured from micro-CT images of actual Fontainebleau samples (Suzanne, 2003; Suzanne et al., 2003b). Properties of the reconstructions and the extracted pore-networks are summarized in Tables 2 and 3. We use the same fluid properties as those reported by Suzanne et al. (2003b). S_{gi} was established by simulating a primary drainage process (injecting gas) in a network initially fully saturated with brine until all the pores are invaded by gas. Then, the imbibition sequence was simulated.

Fig. 8 compares simulated and experimental S_{gr} values as a function of porosity for several Fontainebleau sandstone samples. The stochastic models over-estimate trapping while the new PBF

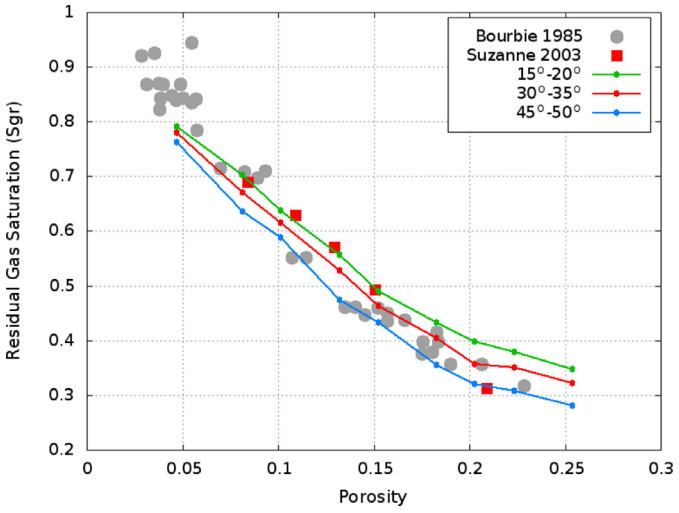

Fig. 9. Sensitivity analysis of advancing contact angles on capillary trapping for different Fontainebleau sandstone samples, compared with experimental data from Bourbie and Zinzner (1985) and Suzanne et al. (2003b).

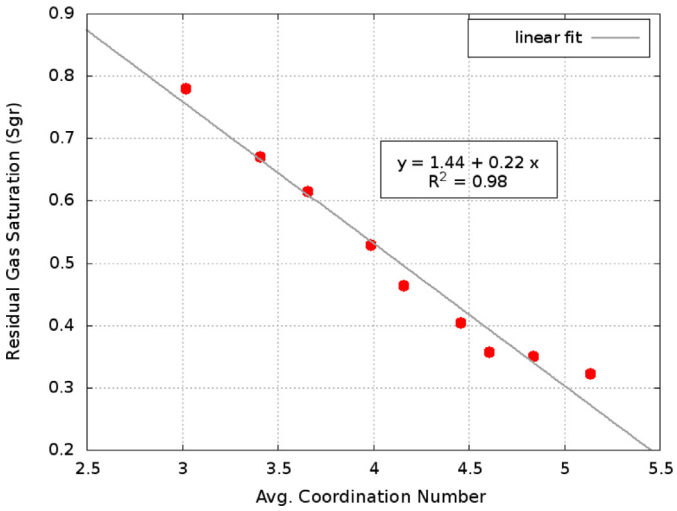

Fig. 10. Simulated residual saturation versus average coordination number for Fontainebleau sandstone.

model describes more accurately the experimental data, especially at high porosities. The displacement statistics show that snap-off is the dominant bond-breaking mechanism for the new model. Snap-off and PBF have similar frequencies for the stochastic models. At low porosities ($\phi < 0.12$), there is little difference between the models. Nie et al. (2016) simulated imbibition directly on micro-CT images of Fontainebleau sandstone using a two-phase lattice Boltzmann method. As shown in Fig. 8, the discrepancies in S_{gr} for these direct simulations are larger than those for the network model simulations across the entire porosity range.

Fig. 9 shows the effects of contact angles on the simulated S_{gr} versus porosity curve. The variation in trapped gas saturation with contact angle is more pronounced at high porosities. Low contact angles favor snap-off (Øren et al., 1998) and we see more trapping. At low porosities, changing the contact angle in the range considered here has little effect on trapping.

The pore-throat aspect ratio for the Fontainebleau networks changes only slightly with porosity ($2.44 < \overline{AR} < 2.73$). This suggests that other geometrical properties of the pore structure control the significant effects of porosity on trapping. Obviously, the connectivity or average coordination number changes with porosity. For the nine networks analyzed here, $\bar{z}$ decreases strongly with porosity and varies in the range $3.02 < \bar{z} < 5.14$ (see Table 3). As shown in Fig. 10, the average coordination number and trapped gas saturation are clearly correlated. The correlation coefficient between S_{gr} and $\bar{z}$ is 0.98.

Suzanne et al. (2003a,b) and Suzanne (2003) measured relationships between trapped gas saturation and initial gas saturation using several samples of Fontainebleau sandstone. The results of two of those samples are used in this section. The porosities of the samples were 0.15 and 0.13, with corresponding permeabilities of 1660 and 880 mD, respectively. We compare the experimental data with simulated results using the Fontainebleau_6 network which has a porosity of 0.129.

Fig. 11 displays the simulated and measured trapping curves. The stochastic models over-predict S_{gr} across the entire saturation range. The results for the new PBF model are more consistent with the experimental data. The ratio of snap-off to I_n events is highest for the new PBF model and, similar to the sandpack results, the amount of trapping is smaller than for the stochastic models. Fig. 12 displays the effects of contact angles on the trapping curve. Contact angles have a clear effect on S_{gr} at high initial saturations with increased trapping at smaller contact angles.

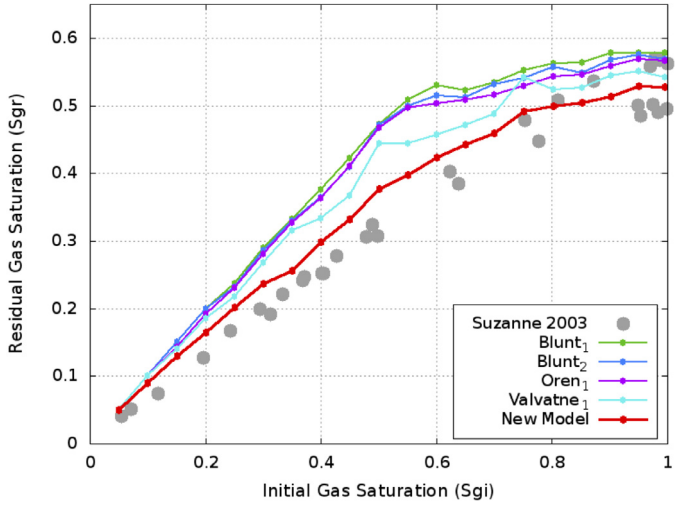

Fig. 11. Comparison between experimental (Suzanne et al., 2003b) and simulated trapping curves for Fontainebleau sandstone.

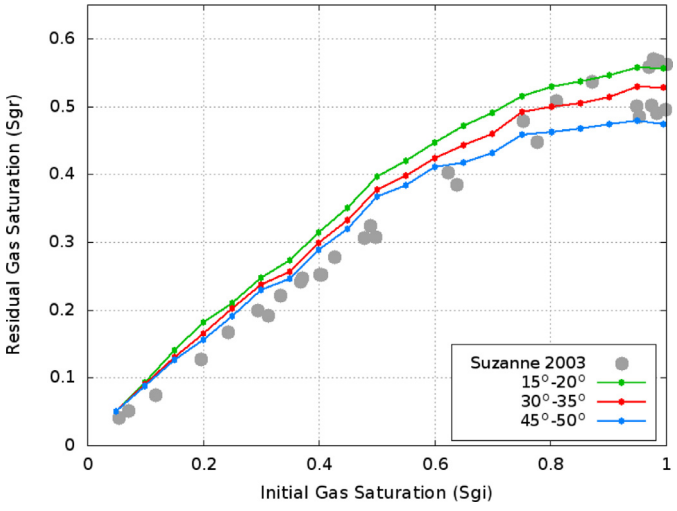

Fig. 12. Sensitivity analysis of advancing contact angles on capillary trapping for Fontainebleau sandstone, compared with experimental data from Suzanne et al. (2003b).

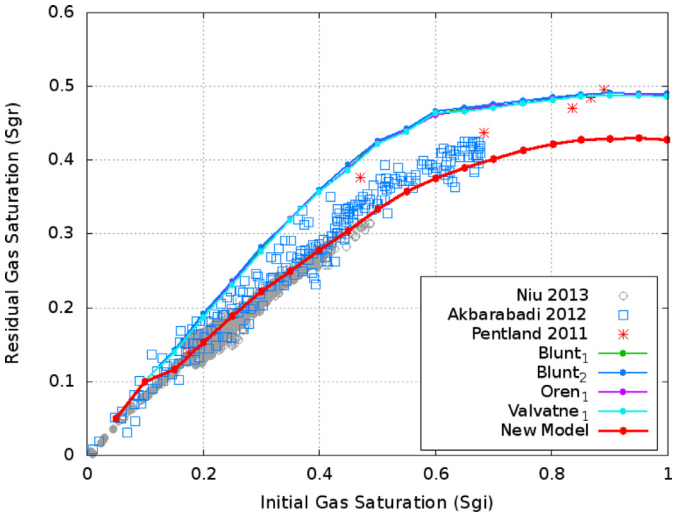

Fig. 13. Comparison between experimental data (Akbarabadi and Piri, 2013; Niu et al., 2015; Pentland et al., 2011) and simulated trapping curves for Berea sandstone.

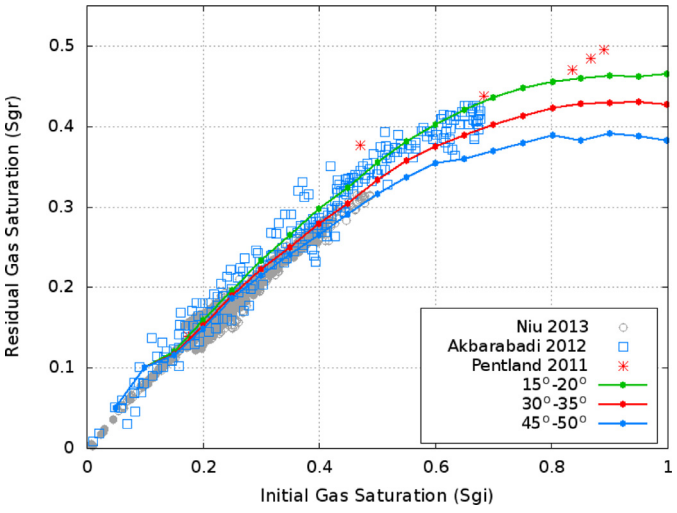

Fig. 14. Sensitivity analysis of advancing contact angles on capillary trapping for Berea sandstone, compared with experimental data from Pentland et al. (2011), Akbarabadi and Piri (2013) and Niu et al. (2015).

5.3. Capillary trapping in Berea sandstone

In this section, we compare experimental trapping data for Berea sandstone (Akbarabadi and Piri, 2013; Niu et al., 2015; Pentland et al., 2011) with simulated results using the different PBF models. Pentland et al. (2011) investigated capillary trapping in an n-decane/brine system. Akbarabadi and Piri (2013) and Niu et al. (2015) reported capillary trapping in CO_2/brine systems. The properties of the rocks and the fluids used in these experiments are presented in Table 1. A process-based model with analogous properties to the Berea sandstone sample described in Pentland et al. (2011) was generated. Tables 2 and 3 list properties of the extracted pore-network.

Fig. 13 compares the simulated and measured trapping curves. As before, the stochastic models over-predict trapping while the new PBF model predicts the measured data more accurately. The stochastic models perform better for Berea sandstone than for the sandpack presented earlier. This is in agreement with the finding of Raeini et al. (2015) and Pentland et al. (2010b). Compared to the sandpack, the Berea network has a wider range of pore and throat sizes and displays a larger average aspect ratio (2.7 vs. 2.0). Snap-off is the dominant trapping mechanism both for the new PBF model and for the stochastic ones. This reduces the differences between the models. The effect of contact angles on the Berea trapping curve is shown in Fig. 14. Trapping increases with decreasing contact angles. The maximum trapped saturation ranges from $S_{gr} \simeq 0.38$ to $S_{gr} \simeq 0.46$ for the contact angles considered here.

5.4. Relative permeability in Berea and Bentheimer sandstones

In this section, the effects of the new PBF model on the relative permeability curves are analyzed. Oak (1990) presented experimental relative permeability curves for three different water-wet Berea sandstone samples. In this work, only the results of the most permeable sample are used (referred to as sample 13 in Oak (1990)). We use the pore-network model described previously in the literature (Lerdhal et al., 2000; Raeesi et al., 2013; Valvatne and Blunt, 2004). This network is a good representation of the Berea sandstone sample used in the experiments. The porosity and permeability of the pore-network are similar to the experimentally reported values. Primary drainage simulations are performed with receding angles in the range 0°–10°. For the imbibition simulation, we assign advancing contact angles in the range 25°–35°, corresponding to the values presented in Section 4.

Fig. 15 compares simulated and measured imbibition relative permeability curves. A significant difference in the trapped oil saturation is observed between the stochastic models and the new PBF model. The stochastic models over-estimate the residual saturation by at least 15%. The new model describes more accurately the residual saturation and the experimental relative permeability curves. Several works have used the same pore-network and reproduced the experimental data by adjusting the advancing contact angle to unrealistically high values: 30°–57° in Lerdhal et al. (2000), 62°–81° in Valvatne and Blunt (2004) and 63°–80° in Piri and Blunt (2005). In this work, the advancing angles are chosen according to the *in-situ* contact angle measurements for a water-wet Berea sandstone reported in Aghaei and Piri (2015).

Alizadeh and Piri (2014) reported steady state relative permeability curves for two- and three-phase systems in a water-wet Bentheimer sandstone sample. An end-cut of the core plug was scanned in a micro-CT scanner at 2.03 µm voxel size. A pore-network representation of the Bentheimer sample was extracted from the micro-CT volume. Properties of the images and pore-network are given in Tables 2 and 3. In the primary drainage simulations, receding contact angles are distributed between 10° and 32°, while for imbibition the advancing contact angles are in the range 20°–42°. These contact angles were measured by Aghaei and Piri (2015) in the same sample of Bentheimer sandstone as used for the relative permeability measurements.

Fig. 16 shows the simulated and measured imbibition relative permeability curves. All the stochastic models over-estimate the trapped oil saturation with about 25%. In addition, the shape of the oil relative permeability curves do not describe the trend observed in the experimental data. The new PBF model predicts more accurately the residual oil saturation and gives a better description of the oil relative permeability shape at high *Sw*. A general over-prediction of the oil relative permeability is observed at low water saturations for all the models. The new model describes the water relative permeability with less than 5% deviation.

5.5. Capillary pressure scanning curves in Bentheimer sandstone

Raeesi (2012) and Raeesi et al. (2013) presented capillary pressure hysteresis curves for two-phase air-water systems in a strongly water-wet Bentheimer sandstone. The experiments included primary drainage, imbibition and secondary drainage scanning curves for different initial saturations. As there are no avail-

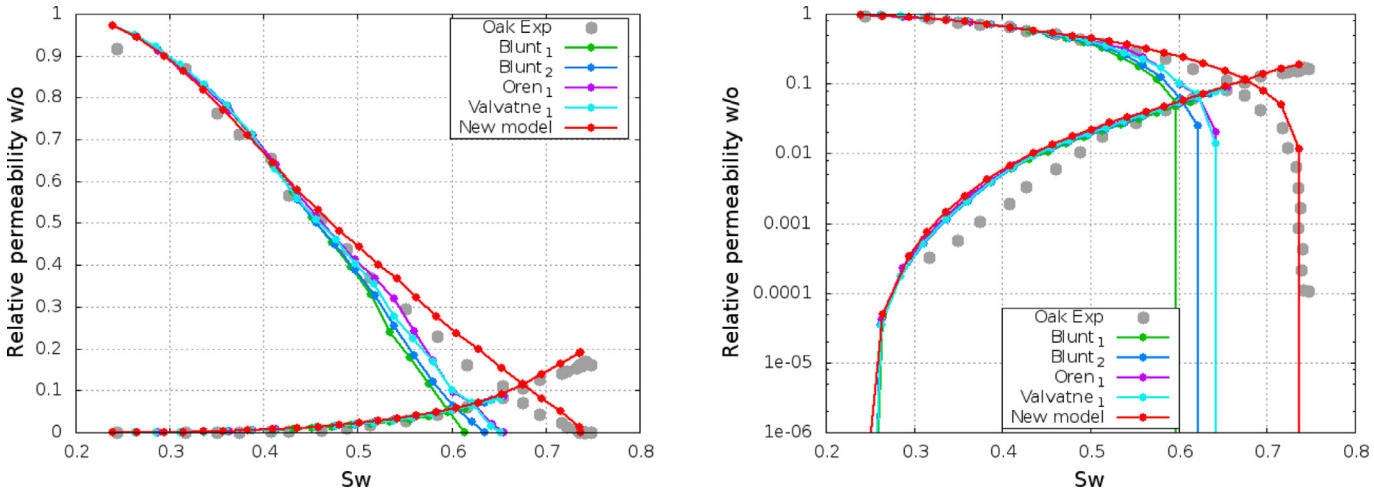

Fig. 15. Comparison of Berea imbibition relative permeability curves for the different PBF models and the experimental results (Oak, 1990).

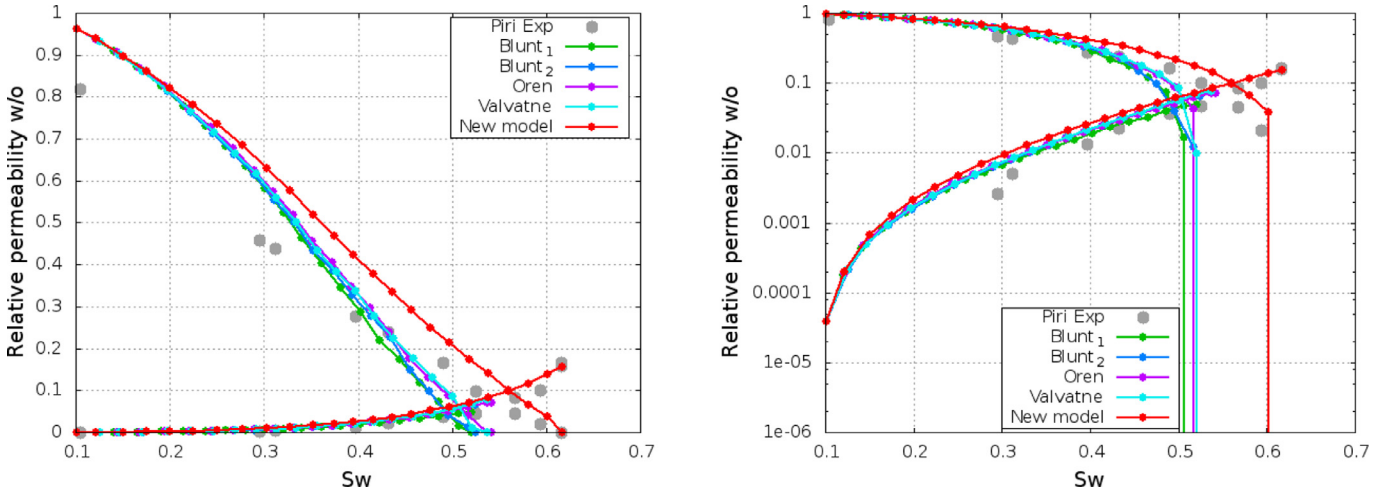

Fig. 16. Comparison of Bentheimer imbibition relative permeability curves for the different PBF models and experimental results (Alizadeh and Piri, 2014).

able pore-space images of the sample used in the experiments, the pore-network described in Idowu et al. (2013), for a Bentheimer sandstone, is used in this section. The properties of this sample are similar to the experimental values reported in Raeesi et al. (2013). The pore-network porosity is 22% while the permeability is 2200 mD. We assign contact angles in the range 0°–10°, 25°–30° and 15°–20° for the primary drainage, imbibition and secondary drainage, respectively.

Simulated capillary pressure scanning curves for three different initial saturations are compared with experimental data in Fig. 17. We note that the simulated primary drainage curve closely follows the experimental one, confirming that throat sizes are captured accurately in the pore-network. The simulated scanning curves reproduce the trapped *nwp* saturations as well as the shape and level of hysteresis seen in the experimental data. Capillary pressure hysteresis is governed by contact angle hysteresis ($\theta_a > \theta_r$), different displacement mechanisms between drainage and imbibition, and trapping of the non-wetting phase. All the stochastic PBF models over-estimated the trapped saturations by at least 20%. Similar findings were reported by Raeesi et al. (2013).

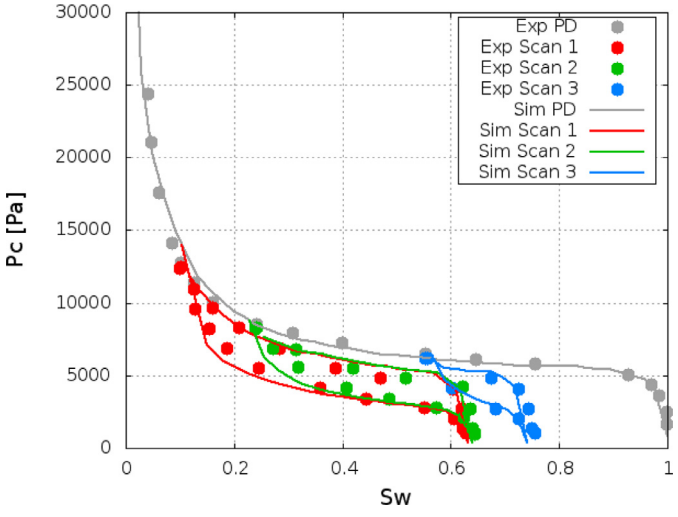

Fig. 17. Comparison of experimental and simulated capillary pressures scanning curves for Bentheimer sandstone.

5.6. Non-wetting phase ganglia size distribution

The pore-scale distribution of trapped non-wetting phase has important implications to enhanced oil recovery, CO_2 storage and gas entrapment in the capillary fringe. Direct 3D micro-CT imaging allows *in-situ* observation of the distribution of the trapped non-wetting phase (Andrew et al., 2013; Favetto et al., 2010; Geistlinger

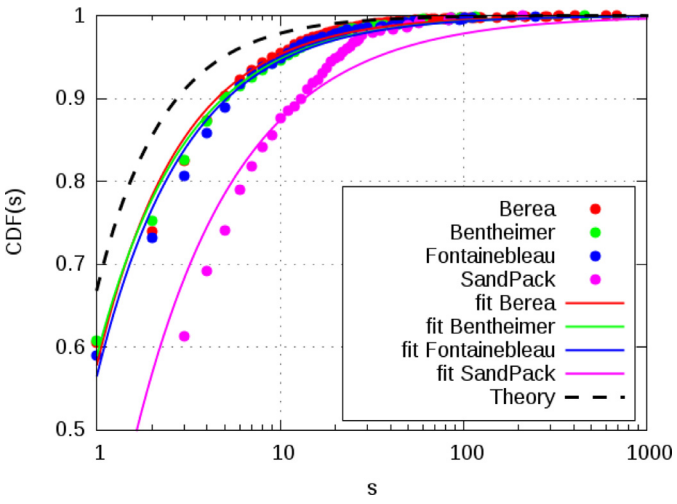

Fig. 18. Cumulative cluster size distribution after imbibition and power law fitting functions for four different samples: Berea, Bentheimer, Fontainebleau_6 sandstones and sandpack.

Table 5
Sensitivity analysis of advancing contact angles on the simulated residual saturations S_{nwr} and the Fisher exponents τ.

Sample	15°–20°		30°–35°		45°–50°	
	S_{nwr}	τ	S_{nwr}	τ	S_{nwr}	τ
Berea	0.46	1.96	0.42	1.92	0.38	1.90
Bentheimer	0.45	1.89	0.38	1.86	0.33	1.85
Fontainebleau_6	0.55	1.90	0.52	1.87	0.47	1.79
Sandpack	0.17	1.76	0.14	1.73	0.13	1.72

and Mohammadian, 2015; Iglauer et al., 2011). In these experiments, trapped *nwp* clusters, or ganglia, of all sizes are observed, from single pore ganglia to multi-pore ganglia that almost span the system. Percolation theory is typically invoked to explain the observed cluster size distribution (Geistlinger and Mohammadian, 2015). As described in Stauffer and Aharony (1994), the cumulative cluster size distribution (*CDF*) is given by

$$CDF(s) = \sum_{1}^{s} PDF(s) = 1 - \left(\frac{k}{s}\right)^{(\tau-1)} \tag{29}$$

where $PDF(s)$ is the probability that a cluster contains s pores, τ is the Fisher exponent and k is a constant. In this work, following percolation theory (Stauffer and Aharony, 1994), s corresponds to the number of sites (pores) in each cluster and not the volume of the cluster as described in Favetto et al. (2010) and Iglauer et al. (2011).

The simulated ganglia size distributions after imbibition for the Berea, Bentheimer, Fontainebleau sandstones and the sandpack are shown in Fig. 18. The three sandstones have similar cluster size distributions. We see a truncated power-law distribution with scaling over approximately three orders of magnitude in ganglion size. A least-square fit to the data yields Fisher exponents in the range $1.89 < \tau < 1.96$ for advancing contact angles between 15° and 20°, as reported in Table 5. These values are smaller than the theoretical value for bond percolation in three-dimensions ($\tau = 2.189 \pm 0.002$ (Lorenz and Ziff, 1998)). As discussed earlier, imbibition in these sandstones proceeds by a combination of snap-off and frontal advance. Piston-like I_1 displacements and cooperative pore-body filling leads locally to well-swept regions of the pore space with little trapping. Physically, this introduces a lower correlation length or cut-off length for the onset of percolation-type behavior (Blunt and Scher, 1995).

As shown in Fig. 18, the behavior of the sandpack is different from the other samples. The cluster size distribution is not well described by a power law. There are considerably fewer smaller blobs than would be predicted by percolation theory and most of the residual non-wetting phase saturation is dominated by the largest clusters. Imbibition in the sandpack advances by a subtle balance between snap-off and I_1 piston-like displacements which leads to a flat frontal advance with very little trapping. Snap-off (bond percolation) is not the main trapping mechanism and the process cannot be described by percolation theory. This is reflected by a lower Fisher exponent, $\tau = 1.76$.

The results presented in the previous sections demonstrated that the relative importance of snap-off and cooperative pore-body filling depends on the contact angle. This implies that the distribution of the trapped non-wetting phase, and therefore the exponent τ, are sensitive to the contact angle. This is confirmed by the results listed in Table 5. For all the samples, the value of the residual *nwp* saturation S_{nwr} and the Fisher exponent τ decrease as the contact angles increase. The frequency of small clusters gradually decreases with increasing contact angles. Higher contact angles impede snap-off and local disconnection of the non-wetting phase is suppressed by frontal advance and cooperative pore-body filling.

6. Conclusion

We present a new model to describe cooperative pore-body filling in geologically realistic pore-networks. The model accounts for geometrical characteristics of the pore-body, the spatial locations of the connecting throats and the local fluid topology. The main geometrical assumption is that the center-line of the throats connected to a pore meet in the center of the pore.

We validate the model by comparing simulated capillary trapping curves with published data for four water-wet samples (sandpack, Berea, Fontainebleau and Bentheimer). The simulations are performed on pore-networks extracted from micro-CT images or process-based reconstructions of the actual rock samples used in the experiments. Published *in-situ* measured contact angle distributions are used as input to the pore-scale simulations.

We predict capillary trapping curves that are in good agreement with the experimental data for all of the four samples. The new PBF model predicts more accurately residual non-wetting phase saturations compared with commonly used stochastic models. In particular, we successfully compute the trapping curve for a sandpack which could not be matched previously using stochastic pore-body filling models, regardless of the contact angle assumed (Raeini et al., 2015). We attribute this to a more accurate description of the cooperative pore-body filling displacement mechanism. We show that trapping in the sandpack is controlled by a subtle balance between snap-off events and frontal I_1 piston-like advance. These subtleties are not captured when using the stochastic pore-body filling models. The new model successfully predicts capillary pressure scanning curves and imbibition relative permeability for Bentheimer sandstone using *in-situ* measured contact angles as input to the simulations.

The non-wetting phase is trapped in clusters of all sizes, from single pore blobs to large multi-pore blobs. The amount and distribution of trapped non-wetting phase is determined by the relative importance of snap-off (bond percolation) and frontal advance. The simulated cluster size distributions have a lower Fisher exponent than predicted by percolation theory. Cooperative pore-body filling and piston-like I_1 displacements introduce a lower cut-off length for percolation-like behavior. The simulated frequency of

small blobs is less than the theoretical value predicted from percolation theory.

Acknowledgments

The authors would like to acknowledge Professors M. Piri and M. Blunt for the micro-CT images of the Bentheimer sandstone and sandpack models. Kurdistan Chawshin is thanked for helping with the generation of the Berea models. In addition, Alexandra Golab is thanked for her helpful comments on this manuscript. The authors wish to acknowledge financial assistance provided through Australian National Low Emissions Coal Research and Development (Grant 7-0311-0128).

Appendix A. The effects of ϵ on predicted trapping

We performed a sensitivity analysis of the amount of trapping predicted by the new PBF model to the exact value of the parameter ϵ in Eq. (12). Three different cases were analyzed: *non-invasive* $\epsilon = 0.0$, *full-invasive* $\epsilon = 1.0$, and $\epsilon = 0.5$. We note that in the *non-invasive* limit, $\gamma = \gamma_{max}$ and Eq. (16) simplifies to

$$R_n = \frac{\tan(\frac{\alpha}{2})}{\sin(\beta)}\left(\frac{r_t}{\sin(\frac{\alpha}{2})} + r_p \cos\left(\frac{\gamma}{2}\right)\right) \tag{A.1}$$

where the R_n is the radius of curvature of the interface.

The differences in predicted residual saturations between the three cases are smaller than 5% for most of the samples. However, larger differences can be observed in samples with a fine balance between snap-off and PBF. This is illustrated in Fig. A.19 which shows the sensitivity of the sandpack trapping curve to the value of ϵ. There is little difference in trapping between the cases $\epsilon = 1.0$ and $\epsilon = 0.5$. Generally, the amount of trapping varied less than 2% between these cases. However, in the limiting case of $\epsilon = 0.0$, the simplified Eq. (A.1) can predict up to 15% less trapping at high initial saturations, as shown in Fig. A.19.

For all the simulations in this work we used $\epsilon = 0.5$. Geometrically, this corresponds to the case where the invading interface becomes unstable at the mid-point of the throat (i.e. between point P_w and L_w in Fig. 1).

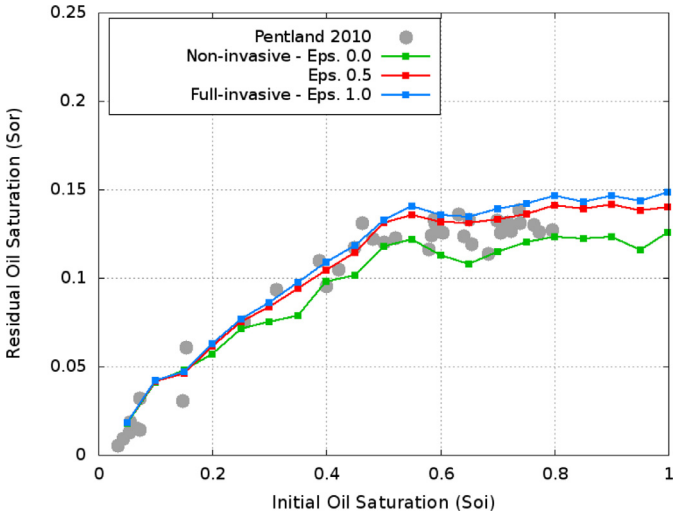

Fig. A.19. Sensitivity analysis of the parameter ϵ, in Eq. (12), on capillary trapping for a sandpack. Experimental capillary trapping data from Pentland et al. (2010a).

References

Aghaei, A., Piri, M., 2015. Direct pore-to-core up-scaling of displacement processes: dynamic pore network modeling and experimentation. J. Hydrol. 522, 488–509.
Akbarabadi, M., Piri, M., 2013. Relative permeability hysteresis and capillary trapping characteristics of supercritical CO_2/brine systems: an experimental study at reservoir conditions. Adv. Water Resour. 52, 190–206.
Akbarabadi, M., Piri, M., 2015. Co-sequestration of SO_2 with supercritical CO_2 in carbonates: an experimental study of capillary trapping, relative permeability and capillary pressure. Adv. Water Resour. 77, 44–56.
Al-Mansoori, S.K., Itsekiri, E., Iglauer, S., Pentland, C.H., Bijeljic, B., Blunt, M., 2010. Measurements of non-wetting phase trapping applied to carbon dioxide storage. Int. J. Greenhouse Gas Control 4, 283–288.
Al-Raoush, R.I., Wilson, C.S., 2005. A pore-scale investigation of a multiphase porous media system. J. Contam. Hydrol. 77, 67–89.
Alizadeh, A.H., Piri, M., 2014. The effect of saturation history on three-phase relative permeability: an experimental study. Water Resour. Res. 50.
Andrew, M., Bijeljic, B., Blunt, M.J., 2013. Pore-scale imaging of geological carbon dioxide storage under in-situ conditions. Geophys. Res. Lett. 40, 3915–3918.
Andrew, M., Bijeljic, B., Blunt, M.J., 2014a. Pore-scale contact angle measurement at reservoir conditions using X-ray microtomography. Adv. Water Resour. 68, 24–31.
Andrew, M., Bijeljic, B., Blunt, M.J., 2014b. Pore-scale imaging of trapped supercritical carbon dioxide in sandstones and carbonates. Int. J. Greenhouse Gas Control 22, 1–14.
Andrew, M., Menke, H., Blunt, M.J., Bijeljic, B., 2015. Dynamic drainage and imbibition imaged using fast X-ray microtomography. SCA.
Armstong, R., Berg, S., 2013. Interfacial velocities and capillary pressure gradients during haines jumps. Phys. Rev. E 88.
Armstrong, R.T., Georgiadis, A., Ott, H., Klemin, D., Berg, S., 2014. Critical capillary number: desaturation studied with fast X-ray computed microtomography. Geophys. Res. Lett. 41, 55–60.
Armstrong, R.T., Porter, M.L., Wildenschild, D., 2012. Linking pore-scale interfacial curvature to column-scale capillary pressure. Adv. Water Resour. 46, 55–62.
Bakke, S., Øren, P.E., 1997. 3D pore-scale modeling of sandstones and flow simulations in the pore networks. SPE J. 2, 136–149.
Bear, J., 1988. Dynamics of Fluids in Porous Media. Dover, New York.
Berg, S., Ott, H., Klapp, S.A., Schwing, A., Neitler, R., Brusse, N., Makurat, A., Leu, L., Enzmann, F., Schwartz, J.-O., Kersten, M., Irvine, S., Stampanoni, M., 2013. Real–time 3D imaging of haines jumps in porous media flow. Proc. Natl. Acad. Sci. USA 110, 3755–3759.
Blunt, M.J., 1997. Pore level modelling of the effects of wettability. SPE J. 2, 494–510.
Blunt, M.J., 1998. Physically-based network modeling of multiphase flow in intermediate-wet porous media. J. Petroleum Sci. Eng. 20, 117–125.
Blunt, M.J., Scher, H., 1995. Pore level modelling of wetting. Phys. Rev. E 52.
Bondino, I., Hamon, G., Kallel, W., Kachuma, D., 2013. Relative permeabilities from simulation in 3D rock models and equivalent pore networks: critical review and way forward. Petrophysics 54, 538–546.
Bourbie, T., Zinzner, B., 1985. Hydraulic and acoustic properties as a function of porosity in Fontainebleau sandstone. J. Geophys. Res. 11524–11532.
Bryant, S., Blunt, M.J., 1992. Prediction of relative permeability in simple porous media. Phys. Rev. A 46, 2004–2011.
Chatzis, I., Morrow, N.R., 1984. Correlation of capillary number relationships for sandstones. SPE J. 24, 555–562.
Chatzis, I., Morrow, N.R., Lim, H., 1983. Magnitude and detailed structure of residual oil saturation. SPE J. 23, 311–326.
Dong, H., Blunt, M.J., 2009. Pore-network extraction from micro-computerized-tomography images. Phys. Rev. E 80, 036307.
Fatt, I., 1956a. The network model of porous media i. capillary pressure characteristics. Trans. AIME 207, 144.
Fatt, I., 1956b. The network model of porous media II. dynamic properties of a single size tube network. Trans. AIME 207, 160.
Fatt, I., 1956c. The network model of porous media III. dynamic properties of networks with tube radious distribution. Trans. AIME 207, 164.
Favetto, S.I.S., Spinelli, G., Schema, G., Blunt, M., 2010. X-ray tomography measurements of power-law cluster size distributions for the nonwetting phase in sandstones. Phys. Rev. E 82.
Geistlinger, H., Mohammadian, S., 2015. Capillary trapping mechanism in strongly water wet systems: comparison between experiment and percolation theory. Adv. Water Resour. 79, 35–50.
Georgiadis, A., Berg, S., Makurat, A., Maitland, G., Ott, H., 2013. Pore scale micro–computed-tomography imaging: nonwetting-phase cluster size distribution during drainage and imbibition. Phys. Rev. E 88, 033002.
Herring, A.L., Harper, E.J., Andersson, L., Sheppard, A., Bay, B.K., Wildenshild, D., 2013. Effect of fluid toplogy on residual nonwetting phase trapping: implications for geologic CO_2 sequestration. Adv. Water Resour. 62, 47–58.
Hilfer, R., Armstrong, R.T., Berg, S., Georgiadis, A., Ott, H., 2015. Capillary saturation and desaturation. Phys. Rev. E 92, 063023.
Hilfer, R., Øren, P.E., 1996. Dimensional analysis of pore scale and field scale immiscible displacement. Transp. Porous Media 22, 53–72.
Hughes, R.G., Blunt, M., 2000. Pore scale modeling of rate effects in imbibition. Transp. Porous Media 40, 295–322.
Idowu, N., Nardi, C., Long, H., Øren, P.E., 2013. Effects of segmentation and skeletonisation algorithms on pore networks and predicted multiphase transport properties on reservoir rock samples. In: SPE Reservoir Characterization and Simulation Conference and Exhibition. Abu Dhabi, United Arab Emirates.

Iglauer, S., Paluszny, A., Pentland, C.H., Blunt, M., 2011. Residual CO_2 imaged with X-ray micro-tomography. Geophys. Res. Lett. 38.
Jadhunandan, P., Morrow, N.R., 1995. Effects of wettability on waterflood recovery for crude-oil brine rock systems. SPE Reservoir. Eng. 10, 40–46.
Jerauld, G.R., Salter, J., 1990. The effect of pore-structure on hysteresis in relative permeability and capillary pressure: pore-level modelling. Transp. Porous Media 5, 103–151.
Joekar-Niasar, V., Doster, F., Armstrong, R., Wildenshild, D., Celia, M.A., 2013. Trapping and hysteresis in two-phase flow in porous media: a pore network study. Water Resour. Res. 49, 1–13.
Khishvand, M., Akbarabadi, M., Piri, M., 2016a. Micro-scale experimental investigation of the effect of flow rate on trapping in sandstone and carbonate rock samples. Adv. Water Resour. 94, 379–399.
Khishvand, M., Alizadeh, A.H., Piri, M., 2016b. In-situ characterization of wettability and pore-scale displacements during two- and three-phase flow in natural porous media. Adv. Water Resour. 97, 279–298.
Koroteev, D., Dinariev, O., Evseev, N., Klemin, D., Nadeev, A., Safanov, S., Gurpinar, O., Berg, S., van Kruijsdjik, C., Armstrong, R., Myers, M.T., Hathon, L., de Jong, H., 2013. Direct hydrodynamic simulation of multiphase flow in porous rock. International Symposium of the Society of Core Analysis. California, USA.
Kovscek, A.R., Radke, C.J., 1993. A pore-level scenario for the development of mixed wettability in oil reservoirs. AlChE J. 39, 1072–1085.
Krevor, S.C.M., Blunt, M.J., Benson, S.M., Pentland, C.H., Reynolds, C., Al-Menhali, A., Niu, B., 2015. Capillary trapping from geological carbon dioxide storage - from pore scale physics to field scale implications. Int. J. Greenhouse Gas Control 40, 221–237.
Krevor, S.C.M., Pini, R., Zuo, L., Benson, S.M., 2012. Relative permeability and trapping of CO_2 and water in sandstone rocks at reservoir conditions. Water Resour. Res. 48.
Kumar, M., Senden, T. J., Shepard, A., Middleton, J. P., Knackstedt, M., 2009. Visualizing and quantifying the residual phase distribution in core material. SCA2009-16.
Lake, L., 1989. Enhanced Oil Recovery. Prentice Hall, New York.
Land, C.S., 1968. Calculation of imbibition relative permeability for two-phase and three-phase flow from rock properties. SPE J. 8, 149–156.
Lenormand, R., Zarcone, C., 1984. Role of roughness and edges during imbibition in square capillaries. SPE, 1–17.
Lenormand, R., Zarcone, C., Sarr, A., 1983. Mechanisms of displacement of one fluid by another in a network of capillary ducts. J. Fluid Mech. 135, 337–353.
Lerdhal, T.R., Øren, P.E., Bakke, S., 2000. A predictive network model for three-phase flow in porous media. SPE/DOE Improved Oil Recovery Symposium. Oklahoma, USA.
Lindquist, W.B., Venkatarangan, A., 1999. Investigating 3D geometry of porous media from high resolution images. Phys. Chem. Earth Part A. 24, 593–599.
Lindquist, W.B., Venkatarangan, A., Dunsmir, J., Wong, T.F., 2000. Pore and throat size distributions measured from synchrotron X-ray tomographic images of Fontainebleau sandstones. J. Geophys. Res. Solid Earth 105, 21509–21527.
Lorenz, C.D., Ziff, R.M., 1998. Universality of the excess number of clusters and the crossing probability function in three-dimensional percolation. J. Phys. A 31, 8147.
Mayer, R.P., Stowe, R.A., 1965. Mercury porosimetry-breakthrough pressure for penetration between packed spheres. J. Colloid Interface Sci. 20, 893–911.
Morrow, N.R., Chatzis, I., Tarbert, J.T., 1988. Entrapment and mobilization of waterflood residual oil in bead packs. SPE Reservoir Eng. 3, 927–934.
Nguyen, V.H., Sheppard, A.P., Knackstedt, M.A., Pinczweski, W.V., 2006. The effect of displacement rate on imbibition relative permeability and reisudal saturation. J. Petroleum Sci. Eng. 52, 54–70.
Nie, X., Gundepalli, V., Mu, Y., Sungkorn, R., Toelke, J., 2016. Numerical investigation of oil-water drainage and imbibition in digitized sandstones. Mech. Ind. 17, 202.
Niu, B., Al-Menhali, A., Krevor, S.C., 2015. The impact of reservoir conditions on the residual trapping of carbon dioxide in Berea sandstone. Water Resour. Res. 51, 2009–2029.
Oak, M., 1990. Three-phase relative permeability of water-wet Berea. In: SPE/DOE Enhanced Oil Recovery Symposium. Tulsa, Oklahoma, pp. 109–120.
Øren, P.E., Bakke, S., 2002. Process based reconstruction of sandstones and prediction of transport properties. Transp. Porous Media 46, 311–343.
Øren, P.E., Bakke, S., 2003. Reconstruction of Berea sandstone and pore-scale modelling of wettability effects. J. Petroleum Sci. Eng. 39, 177–199.
Øren, P.E., Bakke, S., Arntzen, O.J., 1998. Extending predictive capabillities to network models. SPE J. 324–336.
Øren, P.E., Bakke, S., Held, R., 2007. Direct pore-scale computation of material and transport properties for North Sea reservoir rocks. Water Resour. Res. 43, 1–11.
Palamara, D.R., Neeman, T., Golab, A.N., Sheppard, A., 2015. A statistical analysis of the effects of pressure, temperature and salinity on contact angles in CO_2-brine-quartz systems. Int. J. Greenhouse Gas Control 42, 516–524.
Patzek, T.A., 2001. Verification of a complete pore network simulator of drainage and imbibition. SPE J. 144–156.
Pentland, C.H., El-Maghraby, R., Iglauer, S., Blunt, M., 2011. Measurements of the capillary trapping of super-critical carbon dioxide in Berea sandstone. Geophys. Res. Lett. 38.
Pentland, C.H., Itsekiri, E., Al-Mansoori, S.K., Iglauer, S., Bijejic, B., Blunt, M., 2010a. Measurements of nonwetting-phase trapping in sandpacks. SPE J. 274–281.
Pentland, C.H., Tanino, Y., Iglauer, S., Blunt, M., 2010b. Capillary trapping in water-wet sandstones: coreflooding experiments and pore–network modeling. In: SPE Annual Technical Conference and Exhibition. Florence, Italy.
Piri, M., Blunt, M.J., 2005. Three-dimensional mixed-wet random pore-scale network modelling of two- and three-phase flow in porous media. II. results. Phys. Rev. E 71, 1–30.
Princen, H.M., 1969. Capillary phenomena in assemblies of parallel cylinders. i. capillary rise between two cylinders. J. Colloid Interface Sci. 30, 69–75.
Raeesi, B., 2012. Measurement and Pore-Scale Modelling of Capillary Pressure Hysteresis in Strongly Water-Wet Sandstones. Ph.D. thesis University of Wyoming, Laramie, USA.
Raeesi, B., Morrow, N., Mason, G., 2013. Pore network modeling of experimental pressure hysteresis relationships. International Symposium of the Society of Core Analysis. California, USA.
Raeini, A.Q., Bijeljic, B., Blunt, M.J., 2015. Modelling capillary trapping using finite-volume simulation of two-phase flow directly on micro-CT images. Adv. Water Resour. 83, 102–110.
Ramstad, T., Varslot, T., Meland, R., Arntzen, O.J., 2014. Effects of wettability and interfacial tension on the distribution of residual oil on the pore scale after waterflooding. International Symposium of the Society of Core Analysis. Avignon, France.
Roof, J., 1970. Snap-off of oil droplets in water-wet pores. SPE J. 10, 85–91.
Ryazanov, A.V., Marinus, I.J., Van Dijke, M.I.J., sorbie, K.S., 2010. Prediction of residual oil saturation in mixed-wet networks using accurate pore shape descriptors. In: XVIII International Conference on Water Resources, CMWR. Barcelona, Spain.
Silin, D., Patzek, T., 2006. Pore space morphology analysis using maximal inscribed spheres. Physica A 371, 336–360.
Spiteri, E.J., Juanes, R., Blunt, M.J., Orr, F.M., 2008. A new model of trapping and relative permeability hysteresi for all wettability characteristics. SPE J. 277–288.
Stauffer, D., Aharony, A., 1994. Introduction to Percolation Theory, Revised second ed. Taylor and Francis, Philadelphia.
Suekane, T., Nobuso, T., Hirai, S., Kiyota, M., 2008. Geological storage of carbon dioxide by residual gas and solubility trapping. J. Greenhouse Gas Control 2, 58–64.
Suekane, T., Zhou, N., Hosokawa, T., Matsumoto, T., 2009. Direct observation of trapped gas bubbles by capillarity in sandy porous media. Transp. Porous Media 82, 111–122.
Suzanne, K., 2003. Evaluation de la Saturation Residuelle en Gaz de Gres Mouillables a l'eau - Influences des Caracteritiques de la Roche et de la Saturation en Gaz. Ph.D. thesis Ecole des Mines de Paris, France.
Suzanne, K., Hamon, G., Billiote, J., Trocme, V., 2003a. Residual gas saturation of sample originally at residual water saturation in heterogenous sandstone reservoirs. SCA International Symposium of the Society of Core Analysts. Pau, France.
Suzanne, K., Hamon, G., Trocme, V., 2003b. Experimental relationships between residual gas saturation and initial gas saturation in heterogeneous sandstone reservoirs. SPE 84038.
Taber, J., 1969. Dynamic and static forces required to remove a discontinuous oil phase from porous media containing both oil and water. SPE J. 9, 3–12.
Valvatne, P.H., 2004. Predictive Pore-Scale Modelling of Multiphase Flow. Ph.D. thesis Imperial College, London, England.
Valvatne, P.H., Blunt, M.J., 2004. Predictive pore–scale modeling of two-phase flow in mixed wet media. Water Resour. Res. 40, 1–21.
Youssef, S., Peysson, Y., Bauer, D., Vizika, O., 2015. Capillary desaturation curve prediction using 3D microtomography images. SCA.
Zuo, L., Benson, S.M., 2014. Process-dependent residual trapping of CO_2 in sandstone. Geophys. Res. Lett. 41, 2820–2826.